PCCP

ROYAL SOCIETY OF CHEMISTRY

PAPER

View Article Online
View Journal

Cite this: DOI: 10.1039/d6cp00414h

Aggregation behavior of sodium caprate under different pH, concentration, and intestinal fluid conditions: a coarse-grained molecular dynamics study comparing Martini 2 and Martini 3

Shahina Akter,[ab] L. Magnus Bergström,[c] Per Hansson,[bc] Shakhawath Hossain *[ab] and Per Larsson *[ab]

Sodium caprate (C10) is an ionizable amphiphile whose self-assembly behavior in aqueous environments is strongly modulated by pH and concentration. Understanding the molecular-level organization and dynamics of C10 under physiologically relevant solution conditions is important for interpreting its functional behavior in complex media. In this study, we investigated the pH- and concentration-dependent aggregation of C10 in the presence and absence of fasted-state simulated intestinal fluid using coarse-grained molecular dynamics (CG-MD) simulations and compared the results with small-angle X-ray scattering (SAXS) and dynamic light scattering (DLS) measurements. Two CG-MD force fields, Martini 2 and Martini 3, were evaluated for their ability to reproduce experimentally observed aggregate structures. Both models captured the expected pH-dependent transition from small micelles at high pH to larger colloidal assemblies at lower pH, with overall good agreement between simulation and experiment. However, clear differences were observed between the force fields: Martini 3 produced SAXS profiles with substantially lower χ^2 values and exhibited a higher proportion of free monomers and more rapid monomer–aggregate exchange, consistent with theoretical expectations for ionizable fatty acids. By assessing both structural correspondence and molecular-level distributions, this work identifies that Martini 3 coarse-grained model effectively captures the pH- and concentration-dependent self-assembly of C10 and provides insights into its underlying molecular mobility.

Received 4th February 2026,
Accepted 11th May 2026

DOI: 10.1039/d6cp00414h

rsc.li/pccp

1. Introduction

Oral administration remains a widely used route for delivering therapeutic compounds due to its convenience, cost-effectiveness, and ease of manufacturing. However, many biologically active molecules exhibit poor stability or low permeability in the gastrointestinal tract, where they encounter enzymatic degradation, pH variations, mucus, and the intestinal epithelium, all of which limit their uptake.[1]

To address these challenges, various strategies have been explored to enhance intestinal absorption. Among these, permeation enhancers (PEs) have received considerable attention due to their ability to modulate epithelial barrier properties and improve transport across the intestinal epithelium.[2,3] Commonly used PEs include medium-chain fatty acids such as sodium caprylate (C8) and sodium caprate (C10),[4] as well as bile salts, acylcarnitines,[5] salcaprozate sodium (SNAC),[6] EDTA,[7] and alkyl maltosides.[6] Although several PE-based formulations have been investigated, only a few PE-based formulations are available in the pharma market, for example, SNAC in oral semaglutide (Rybelsus)[3] and sodium caprylate in oral octreotide (Mycapssa).[8] Currently, C10 is included in the late-stage formulation MK-0616,[9] whereas ORMD-0801[10] relies on other permeation enhancers such as EDTA and bile salts. Notably, the performance of PEs depends strongly on their behavior under physiological conditions; therefore, understanding their physicochemical properties is essential for enabling effective permeation enhancement.

As PEs move through the gastrointestinal environment, they can self-associate to form a range of colloidal structures.[11] Understanding the principles governing this aggregation behavior is therefore essential. At low concentrations, for instance, monomeric C10 interacts primarily with paracellular tight junctions proteins and enhance drug permeability.[8] At higher concentrations, C10 can insert into membranes or form larger aggregates whose structure and dynamics influence interaction

[a] Department of Pharmacy, Uppsala University, 751 23 Uppsala, Sweden. E-mail: shakhawath.hossain@uu.se
[b] The Swedish Drug Delivery Center (SweDeliver), Uppsala University, Uppsala 751 23, Sweden. E-mail: per.r.larsson@uu.se
[c] Department of Medicinal Chemistry, Uppsala University, 751 23 Uppsala, Sweden

mechanisms.[12,13] The size, shape, and organization of these aggregates also affect molecular distribution, diffusion behavior, drug solubilization, and the release profile in solution. Their formation and transformation depend on several factors, including intestinal fluid composition, pH, and the intrinsic physicochemical properties of the PE itself.[14] Because these combined effects are not yet fully understood, predicting aggregation behavior across realistic physiological conditions remains challenging.

In this study, we focused on the aggregation behavior of the medium-chain fatty acid sodium caprate (C10). Within this class of amphiphiles, longer chains such as C12 and C14 have low critical micelle concentrations (CMC), limiting the availability of free monomers,[15] while shorter chains such as C8 have high CMC values but interact less efficiently with lipid environments. C10, with its intermediate chain length, moderate CMC and ability to interact with and increase membrane leakiness, is therefore of particular interest.[12] However, its aggregation behavior is strongly influenced by pH, as the balance between ionized and unionized species changes with both pH and concentration.[16,17] In addition, although C10 has an intrinsic pK_a of around 4.8, self-association causes the apparent pK_a to shift to approximately 7 under certain conditions.[16,18]

A number of different experimental methods have been used to explore the aggregation behavior of C10 and to measure critical micelle concentrations (CMC). For example, Namani and Walde report that C10 forms vesicles within a specific pH range (6.8 to 7.8), and the amount of free decanoate at pH 7.0 is approximately 20 mM.[17] With cryo-TEM, Berg *et al.* report vesicular structures ranging from 50 to several hundred nanometers in diameter for 100 mM C10 in blank fasted state simulated intestinal fluid (FaSSIF).[18] With dynamic light scattering, they observe micelles around 3 nm in diameter with 50 mM C10 at pH 8.5. From this, they conclude that C10 forms micelles at pH 8.5 and vesicles and other larger structures at pH 6.5.[18] However, these experimental methods alone may not fully resolve the molecular-level distribution of molecules between aggregated states and free monomers in solution, as well as the dynamic exchange between these monomeric and aggregated states. A deeper understanding of these inherent molecular-level dynamics is essential for interpreting the *in vivo* performance of C10 and for designing formulations with appropriate C10 concentrations.

To complement experimental approaches, coarse-grained molecular dynamics (CG-MD) simulations provide a useful framework for studying amphiphile self-assembly.[19] By grouping atoms into larger beads, CG-MD simulations simplify the molecular representation, lower computational complexity, and enable the investigation of larger systems over longer time frames.[20,21] Using the CG-MD Martini 2 forcefield, Hossain *et al.*[22] investigated the aggregation behavior of various medium-chain fatty acids and calculated their CMC values. They observed pH-dependent differences in aggregate morphology and size, which were generally consistent with earlier experimental findings and with CMC estimates obtained using the Wilhelmy method. However, the CMC values calculated from the Hossain *et al.*[22] simulations were underpredicted compared to the experimental values by a factor of 1.8 to 3.5. Therefore, while CG-MD can provide valuable molecular-level insights into the aggregation behavior of C10 (and surfactants generally),[19] it is important to critically assess the accuracy of the chosen model. Small-angle X-ray scattering (SAXS) is an experimental method that yields information on the size, shape, and internal structure of aggregates in solution. By integrating CG-MD simulations with SAXS data, researchers can get a complete picture of the aggregation behavior, including the size and structure of the aggregates.[23]

In this work, we combine CG-MD simulations with SAXS and DLS measurements to examine how sodium caprate (C10) aggregates across different pH and concentration conditions, both in the presence and absence of intestinal fluid components. Simulations were performed using the Martini 2 and Martini 3 coarse-grained force fields, and theoretical scattering profiles were generated using PEPSI-SAXS[24] for comparison with experimental SAXS data. In addition to evaluating aggregate structure, we also examined the relative abundance of free monomers in the systems. This molecular-level feature was qualitatively benchmarked against theoretical expectations based on the known solubility and ionization behavior of C10. By considering both structural agreement and molecular-level distributions in comparison with experiment, this study aims to identify the coarse-grained model that most reliably captures the pH- and concentration-dependent self-assembly of the amphiphilic molecule C10 and provides insight into its underlying molecular mobility.

2. Methods

2.1. CG-MD simulations

CG-MD simulations were conducted with the Martini force field (v2[25] and 3[26]), using the Gromacs software. Simulations were made for eight distinct systems (Table 1): two concentrations of C10 (50 and 300 mM) and two pHs values (6.5 and 8.5; these were emulated by simulating different fractions of the C10 protonation states). The Martini 2 molecular topologies were taken from Hossain *et al.* (2019) for C10 and from Clulow *et al.* (2017) for Na-taurocholate; the Martini 3 topologies for the same molecules from Hossain *et al.* 2022.[27,28] For each system, a 30-nm cubic box was created and filled with standard Martini water beads, after which phosphate ions were added to mimic 100 mM phosphate buffer. Then, the desired numbers of C10, Na-taurocholate, and DOPC lipid molecules were added to represent the specific concentrations and compositions presented in Table 1. An equivalent quantity of positively charged sodium ions was also added while using C10 and Na-taurocholate in a charged state to neutralize the system.

Each system then first underwent 10 000 steps of energy minimization using the steepest descent algorithm, followed by equilibration for 500 ps under NVT (constant temperature, constant volume) and NPT (constant temperature, constant pressure) conditions. The v-rescale thermostat was used to

Table 1 Overview of systems simulated with Martini 2 and Martini 3 force fields, including C10 concentration, pH, and medium composition

System	C10 concentration (mM)	Corresponding pH	Medium	Time (μs)	Number of molecules[a]
1	50	6.5	100 mM phosphate buffer	4	W – 203 759, C10 – 812, P – 1630, Na – 3666
2	50	6.5	100 mM phosphate buffer and FaSSIF	4	W – 203 551, C10 – 812, Taur – 48, DOPC – 12, P – 1630, Na – 3714
3	50	8.5	100 mM phosphate buffer	4	W – 203 569, C10 – 812, P – 1630, Na – 4072
4	50	8.5	100 mM phosphate buffer and FaSSIF	4	W – 203 565, C10 – 812, Taur – 48, DOPC – 12, P – 1630, Na – 4120
5	300	6.5	100 mM phosphate buffer	4	W – 203 540, C10 – 4880, P – 1642, Na – 5700
6	300	6.5	100 mM phosphate buffer and FaSSIF	4	W – 203 551, C10 – 4880, Taur – 48, DOPC – 12, P – 1642, Na – 5748
7	300	8.5	100 mM phosphate buffer	4	W – 203 759, C10 – 4880, P – 1630, Na – 5700
8	300	8.5	100 mM phosphate buffer and FaSSIF	4	W – 203 561, C10 – 4880, Taur – 48, DOPC – 12, P – 1630, Na – 5748

[a] To reflect the protonation behavior at different pH levels, C10 molecules were modeled as a 50 : 50 ratio of charged to uncharged species at pH 6.5. In contrast, at pH 8.5 all C10 molecules were fully charged.Abbreviations: FaSSIF-fasted state simulated intestinal fluid, W – water, C10 – Caprate, Na – Sodium ion, P – Phosphate ion.

control the temperature,[29] and an isotropic Berendsen pressure coupling kept the pressure at 1 bar (with a time constant of 12.0 ps and compressibility of 3×10^{-4} bar^{-1}). Following that, production runs for each system were carried out for 4 μs each, using a 10 fs time step.[30]

2.2. Dynamic light scattering

Dynamic light scattering was performed on an ALV/CGS-3/MD-4 Multi-Detection Goniometer System, with ALV/LSE-5004 Light Scattering Electronics Correlator (Germany). Measurements were performed for the sample containing 300 mM sodium caprate (C10) in 0.1 M phosphate buffer at pH 6.5 and 8.5 at 25 °C.

2.3. Small-angle X-ray scattering

Small-angle X-ray scattering (SAXS) experiments were carried out on a Xeuss 2.0 Xenocs X-ray system with a GeniX 3D microfocus X-ray source and a Pilatus3 R 300 K detector without a beam stop at Uppsala University, Sweden. We obtained scattering data for a sample containing 300 mM sodium caprate (C10) in 0.1 M phosphate buffer at pH 6.5 and 8.5. The SAXS measurements were conducted at 25 °C using a 1 mm vacuum capillary, with a sample-to-detector distance of 1015 mm. The background of the samples was subtracted using SASVIEW 5.0.6, and the absolute intensity in cm^{-1} was obtained by dividing that value by the sample thickness.

2.4. Simulation analysis

Simulated trajectories were analyzed with an in-house Python script to determine the number of aggregates and free permeation enhancer monomers. Two separate analyses were conducted, defining the minimum size of an aggregate as containing either five or ten molecules. In both cases, molecules were classified as part of an aggregate if any of their constituent beads were within a cutoff distance (0.5 nm) from another already formed aggregate. Another Python script was used to calculate the number of molecules in each cluster.

To characterize the shape of the aggregates, we calculated the radius of gyration using the ''gmx gyrate'' tool from the GROMACS software package, analyzing each aggregate individually that satisfied the aggregation criterion ($n > 5$ or 10). Based on these results, we then computed the eccentricity values, with lower values indicating more sphere-like aggregate shapes.

The eccentricity values were calculated as

$$E = 1 - \frac{I_{\min}}{I_{\text{avg}}}$$

where $I_{\min}$ and I_{avg} are the minimum and average of the radius of gyration on the x, y, and z axes, respectively.

2.5. Scattering spectra analysis

The simulation trajectories were first back-mapped to all-atom resolution using a modified version of Martini's back-mapping method.[31] Pepsi-SAXS was then used to calculate the scattering intensity curves, $I(q)$, from the simulations, where the momentum transfer $q = 4\pi \sin(\theta)/\lambda$ is provided *via* the wavelength λ and scattering angle 2θ.[24] A structure file and an experimental scattering profile were provided to facilitate the scattering intensity calculation. A constant factor was subtracted during the calculation to account for systematic errors (*i.e.* the standard deviation for the intensity) in the experimental data. Pepsi-SAXS also calculated the goodness of fit Xr^2:

$$Xr^2 = \frac{1}{N-1} \sum \left[\frac{I_{\text{exp}}(q) - I_{\text{theor}}(q)}{\sigma(q)} \right]^2$$

where N is the number of points in the experimental curve, $I_{\text{exp}}(q)$ is the experimental scattering data, $I_{\text{theor}}(q)$ is the theoretical intensity, and $\sigma(q)$ are the experimental errors.

3. Results and discussion

3.1. C10 aggregate morphology and free-monomer fraction in Martini 2 and Martini 3: influence of pH, concentration, and FaSSIF

In this work, we primarily investigated how the choice of coarse-grained Martini force field influences the aggregation behavior of C10 under different physiological conditions

(pH, concentration, and the presence or absence of FaSSIF), while keeping in mind that C10 aggregation is inherently sensitive to these environmental factors. Although pH and concentration strongly affect C10 self-assembly, our results show that the specific version of the Martini force field used in the simulations plays a decisive role in shaping both the extent and morphology of the resulting aggregates.

We simulated C10 systems at two pH conditions, represented by charged : uncharged ratios of 50 : 50 at pH 6.5 and 100 : 0 at pH 8.5, and at two concentrations (50 mM and 300 mM), with and without FaSSIF, as described in Table 1. Since classical molecular dynamics simulations do not explicitly model protonation–deprotonation equilibria, pH effects were approximated by assigning fixed fractions of C10 in its anionic and neutral (protonated) forms. The snapshots from the 4 μs simulations using Martini 3 and Martini 2 are presented in Fig. 1 and 2.

At low pH (50 : 50 ratio), both force fields produced more extensive aggregates. For the 300 mM systems, Martini 3 generated irregular or fiber-like structures (Fig. 1A and C), whereas Martini 2 produced more ordered and compact assemblies, such as vesicles or multilayered structures (Fig. 2A and C). At the lower 50 mM concentration, Martini 3 typically formed one or two micelles in the low-pH system (Fig. 1E and G), with most C10 molecules incorporated into these assemblies. Martini 2, however, produced a large, well-defined vesicle at low pH (Fig. 2E and G).

At high pH (100 : 0 ratio), both force fields showed a shift toward smaller aggregates and a higher proportion of free monomers, consistent with the expected increase in CMC at higher ionization levels. Martini 3 produced small micelles or loosely packed aggregates (Fig. 1B and D), while Martini 2 tended toward more rigid, compact structures, including double bilayers (Fig. 2B and D). At 50 mM, most C10 molecules in Martini 3 remained as free monomers in solution, with only a few small micelles forming. In contrast, in Martini 2, most C10 molecules were incorporated into aggregates even at this lower concentration, leaving very few monomers in solution, and demonstrating Martini 2's tendency to over-stabilize molecular association. Overall, Fig. 1 and 2 shows that both force fields reproduced the expected gross pH-dependent aggregation behavior such as larger aggregates at low pH and smaller micellar structures at high pH, but the structural outcomes differed between them.

The effect of FaSSIF was concentration-dependent for both force fields. At 50 mM, FaSSIF reduced the number of free monomers, promoting additional micellization or incorporation into mixed structures. At 300 mM, however, FaSSIF had minimal impact for either force field, likely because C10 self-association dominated over interactions with bile components due to the high surfactant concentration.

To further quantify these observations, Fig. 3 presents the average percentage of free C10 monomers calculated over the final 2 μs of each simulation for Martini 2 (Fig. 3A) and Martini 3 (Fig. 3B). Martini 3 consistently exhibited a substantially higher proportion of free monomers across all conditions, whereas Martini 2 produced only minimal amounts. These simulation values can be qualitatively benchmarked against theoretical expectations derived from experimental solubility data. Using the caprate solubilities reported by Dahlgren *et al.*[32]

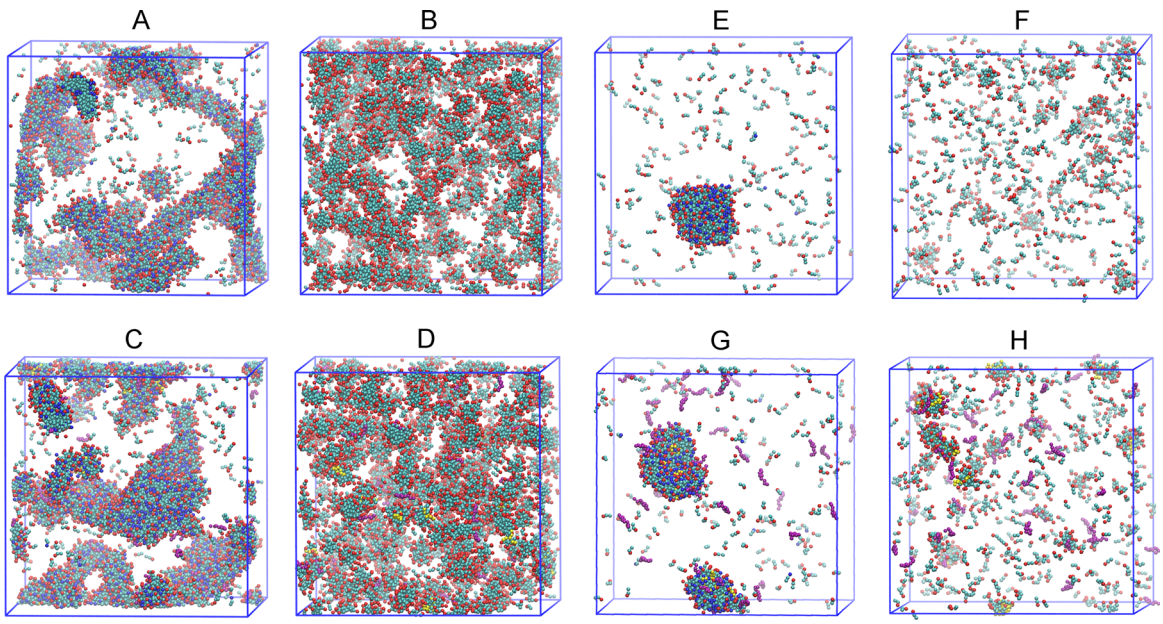

Fig. 1 Simulation snapshots of C10 in phosphate buffer, with and without FaSSIF, using the Martini 3 force field. (A) and (B) depict 300 mM C10 at charged and uncharged ratios of 50 : 50 and 100 : 0, respectively, while (C) and (D) show the same system with the addition of FaSSIF. Similarly, (E) and (F) represent 50 mM C10 at 50 : 50 and 100 : 0 charged and uncharged ratios, respectively, and (G) and (H) include FaSSIF under these conditions. Red beads indicate charged head groups, blue beads represent uncharged head groups, cyan beads correspond to fatty acid chains, yellow beads denote DOPC molecules, and purple beads signify Na-taurocholate molecules.

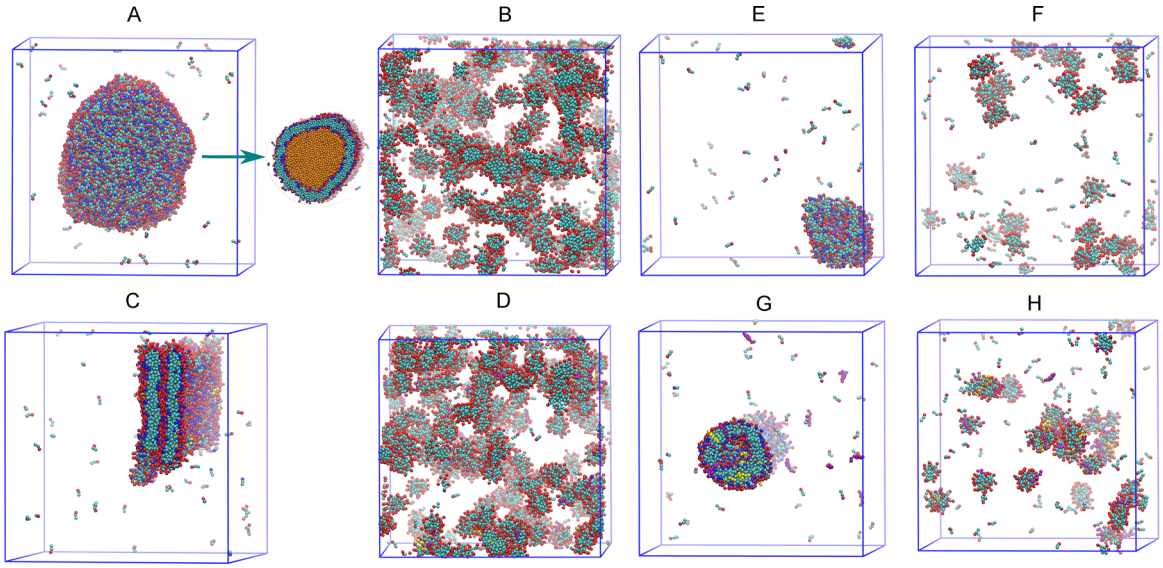

Fig. 2 Simulation snapshots of C10 in phosphate buffer, with and without FaSSIF, modeled with the Martini 2 force field. (A) and (B) depict 300 mM C10 at charged and uncharged ratios of 50 : 50 and 100 : 0, respectively, while (C) and (D) show the same system with the addition of FaSSIF. Similarly, (E) and (F) represent 50 mM C10 at 50 : 50 and 100 : 0 charged and uncharged ratios, respectively, and (G) and (H) include FaSSIF under these conditions. Red beads indicate charged head groups, blue beads represent uncharged head groups, cyan beads correspond to fatty acid chains, yellow beads denote DOPC molecules, purple beads signify Na-taurocholate, and orange beads represent water molecules.

(5 mg mL^{-1} at pH 7.4 and 2 mg mL^{-1} at pH 6.5), our 50 mM and 300 mM systems are expected to contain ~20% and ~4% at low pH, and at least ~50% and ~9% free monomers at high pH, respectively. Since our simulations were performed at pH 8.5, the fraction of free monomers should be even higher than the estimates based on pH 7.4. Martini 3 closely follows these magnitudes: at low pH it predicts approximately 22% and 4% free monomers for the 50 mM and 300 mM systems, respectively, and at high pH it yields about 70% and 11%. In contrast, Martini 2 substantially underestimates the free fraction across both concentrations. At low pH, it predicts only ~5% and ~1% free monomers for the 50 mM and 300 mM systems, respectively, and at high pH it yields just ~12% and ~1.5%. These values are far below the solubility-based expectations and show minimal sensitivity to changes in pH.

Overall, although pH, concentration, and the presence of FaSSIF strongly influence C10 aggregation, our results demonstrate that the choice of a particular Martini force field itself is a decisive factor in determining aggregate size, morphology, and the balance between monomeric and aggregated states. In comparison with Martini 3, Martini 2 was consistently more prone to aggregation, producing larger and more structured assemblies and leaving markedly fewer free monomers in solution. This behavior was evident both in the simulation snapshots and in the quantitative analysis of monomer populations. These trends align with previous reports indicating that Martini 2 tends to over-aggregate[33] and underestimates the critical micelle concentration (CMC) of medium-chain fatty acids by a factor of 1.8–3.5 relative to experiment,[22] reflecting an inherent tendency of Martini 2 beads to interact too strongly.[34–36] Such overly attractive interactions often lead to artificial clustering, exacerbated by relatively weak bonded force constants.[37] In contrast, Martini 3 addresses these limitations through a reparametrized interaction framework, including new bead sizes, chemically diverse bead types, and refined Lennard-Jones parameters.[38] Together, these improvements reduce excessive aggregation and yield a more realistic representation of C10 self-assembly across different physiological conditions.

3.2. Size and number of C10 aggregates in Martini 2 and Martini 3: effects of pH, concentration, and FaSSIF

We then examined how the number and size of C10 clusters evolved over the course of the simulations by monitoring the number of molecules within each cluster (Fig. 4 and Fig. S1). To test the sensitivity of the analysis, two cluster definitions were used: one requiring a minimum of five molecules per cluster, and another requiring at least ten.

For the systems containing 300 mM C10, Fig. 4A and B show the number of clusters over time for the five-molecule and ten-molecule cluster definitions, respectively. In both Martini 2 and Martini 3, the systems reached a relatively steady state after ~500 ns. However, large differences emerged between systems depending on the charged:uncharged ratio. At low pH (50 : 50), only one to twelve clusters were present across the simulations, and this number remained stable throughout. In contrast, when all C10 molecules were fully charged (100 : 0), the number of clusters increased dramatically—reaching approximately 100–250. Notably, Martini 3 consistently produced nearly twice as many clusters as Martini 2 under these conditions (Fig. 4A and B and Fig. S1C and D).

The 50 mM C10 systems (Fig. 4C and D) also showed clear differences between low and high pH. For the 50 : 50 ratio, steady-state behavior was reached between 1500–2500 ns,

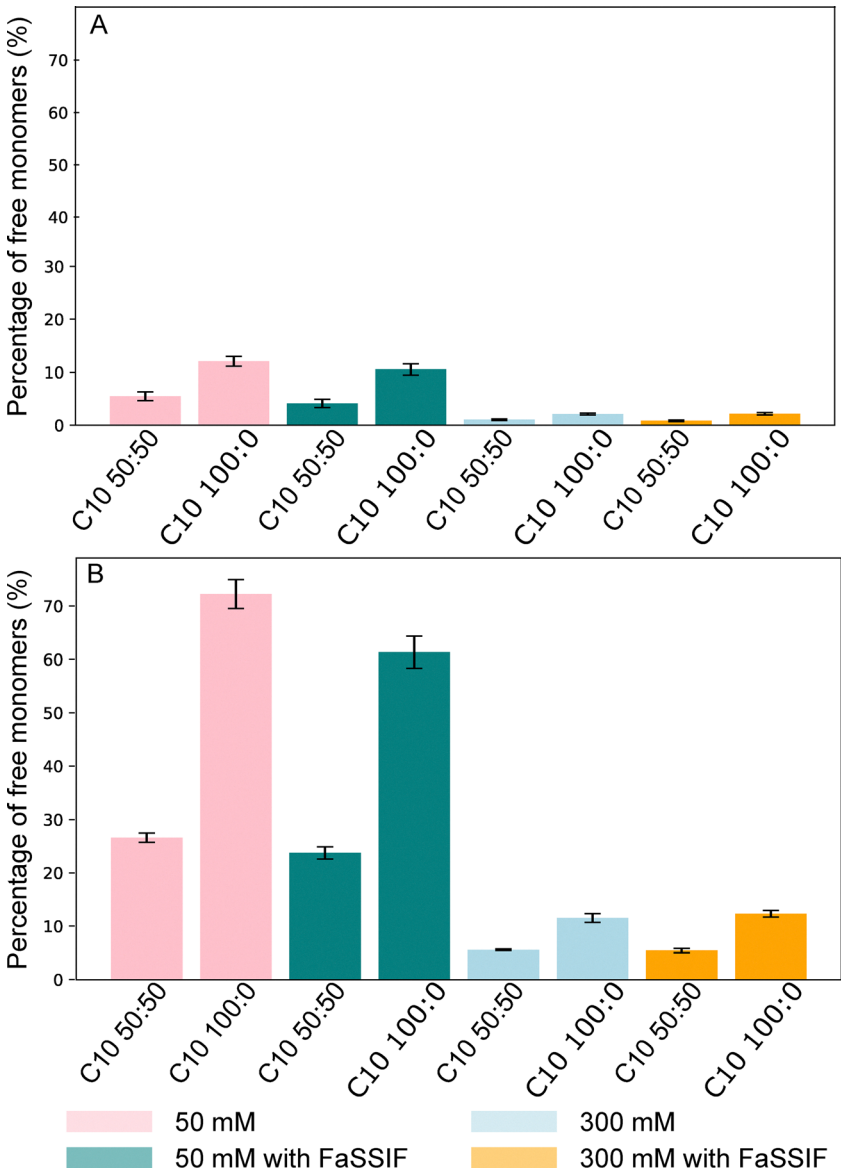

Fig. 3 Average percentage of free monomers in different systems for (A) Martini 2, and (B) Martini 3. The standard deviation around the mean of the percentage values is indicated.

depending on the system, with only one to three clusters present at the end of the 4 μs simulations. In contrast, systems containing only charged C10 exhibited strongly fluctuating cluster numbers over time, indicating dynamic formation and dissociation of aggregates. For both force fields, cluster counts stabilized within 100–200 ns regardless of whether the minimum cluster size was defined as five or ten molecules. Initial differences in cluster numbers were observed only in the 300 mM systems. Importantly, FaSSIF did not influence the number of clusters in this time-evolution analysis.

To further characterize the aggregate structures, we examined the number of C10 molecules in each cluster using the final snapshots of the trajectories (Fig. S1). For 300 mM C10 at low pH (50 : 50), Fig. S1A and B show that Martini 2 formed a single dominant cluster containing approx. 99% of all molecules, with no observable effect from FaSSIF. In contrast, Martini 3 formed multiple clusters, and the presence of FaSSIF doubled the number of clusters while reducing the number of molecules in the largest cluster by ∼33%. For 300 mM C10 at high pH (100 : 0) (Fig. S1C and D), both force fields produced many clusters. However, Martini 2 generated clusters with more molecules per cluster, whereas Martini 3 produced about twice as many clusters, each containing fewer molecules.

At 50 mM C10 and low pH (50 : 50), Fig. S1E and F show that the clustering patterns followed trends similar to those at 300 mM: Martini 2 formed a single large cluster, while Martini 3 formed multiple smaller clusters. In the presence of FaSSIF, Martini 3 formed three clusters, each containing fewer molecules compared to the corresponding systems without FaSSIF. Finally, for 50 mM C10 at high pH (100 : 0) (Fig. S1G and H),

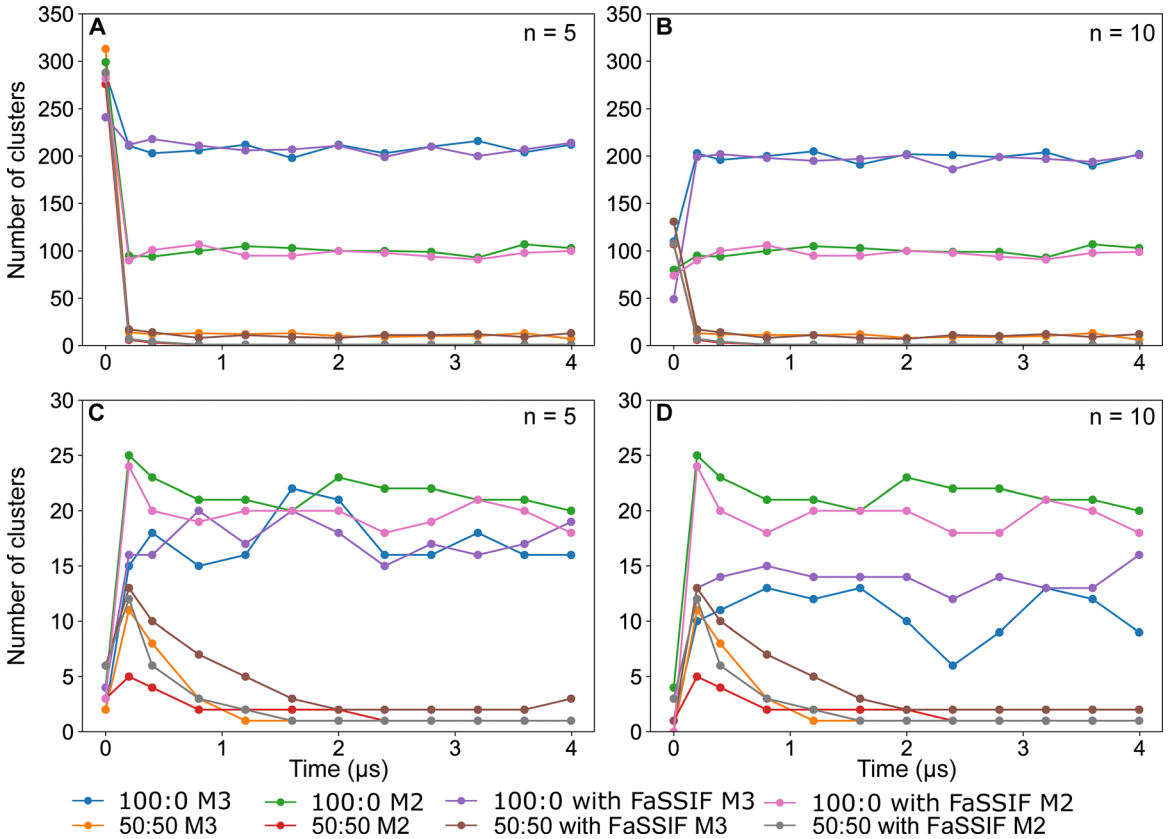

Fig. 4 Cluster sizes for systems studied using Martini 2 (M2) and Martini 3 (M3). (A) and (B) represent the 300 mM system with clusters of five (n = 5) and ten (n = 10) molecules, respectively, at charged-to-uncharged ratios of 100 : 0 and 50 : 50, analyzed with and without FaSSIF. (C) and (D) correspond to the 50 mM system.

Martini 2 and Martini 3 produced a similar number of clusters; however, Martini 2 consistently produced clusters containing more molecules per aggregate, while Martini 3 formed smaller clusters overall.

In summary, Fig. 4 and Fig. S1 demonstrate that the number of clusters increases markedly at high pH, while the size of clusters (number of molecules per cluster) is substantially larger at low pH. Across conditions, Martini 2 forms aggregates containing nearly twice as many molecules as those formed in Martini 3, consistent with the stronger aggregation propensity discussed in Section 3.1. Importantly, an effect of FaSSIF was evident in both cluster count and cluster size—but primarily in the Martini 3 systems, where the presence of intestinal fluid components reduced cluster size and increased the number of clusters.

3.3. Martini 2 and Martini 3 show distinct differences in spherical clustering behavior at higher pH

To compare how the two force fields capture aggregate morphology at higher pH, we calculated the eccentricity values for systems with a charged–uncharged ratio of 100 : 0, as shown in Fig. 5A (Martini 2) and Fig. 5B (Martini 3). Eccentricity provides a quantitative measure of shape, where lower values indicate aggregates that more closely approximate perfect spheres. The distribution in each panel illustrates how frequently aggregates fall within different eccentricity ranges, enabling direct comparison of the two models.

Although both force fields produced predominantly low eccentricity values, indicating a general tendency toward spherical aggregates at higher pH, the overall distributions differed markedly. Martini 2 predicted a substantially higher proportion of nearly spherical clusters, with roughly 35–40% of aggregates showing very low eccentricity values, whereas Martini 3 produced only about 22% spherical clusters within the same range. This difference indicates that Martini 2 favors tighter, more compact micelle formation, while Martini 3 yields a wider variety of shapes.

The concentration dependence of spherical clustering further differentiates the two models. In the Martini 2 systems, the fraction of near-perfect spheres decreased as the C10 concentration increased, suggesting that higher concentrations promote more elongated or irregular structures. In contrast, Martini 3 displayed the opposite trend, with an increase in spherical aggregates at higher C10 concentration. These opposite concentration effects underscore a fundamental difference in how the two force fields describe micelle packing and structural rearrangement.

FaSSIF also influenced aggregation morphology in force-field-specific ways. In Martini 2, the presence of FaSSIF increased the fraction of spherical clusters at both concentrations, with the

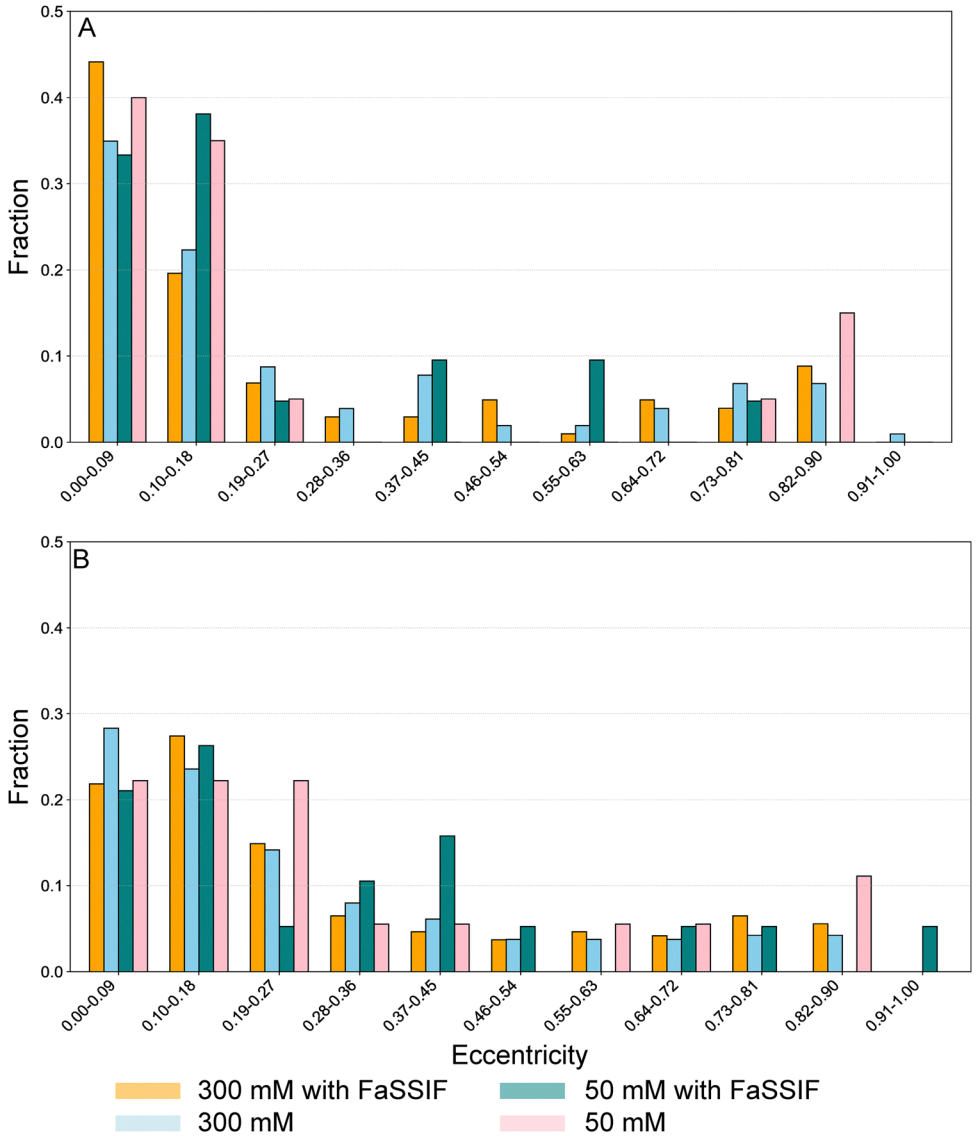

Fig. 5 Eccentricity distributions for systems with charged-uncharged ratios of 100 : 0 as determined with (A) Martini 2, and (B) Martini 3. Each bar represents the fraction of values within the corresponding eccentricity range.

enhancement being most pronounced at high concentration. Martini 3, however, showed an inverse response at high C10 concentration, where the addition of FaSSIF reduced the proportion of spherical aggregates. Despite these variations, both Martini 2 and Martini 3 generated a small population of highly non-spherical structures, with approximately 10% of aggregates exhibiting eccentricity values above 0.82, indicating elongated or irregular morphologies.

3.4. Molecular exchange dynamics reveal mechanistic differences between force fields and their relevance to permeation enhancement

To quantify the molecular-level dynamics of C10 aggregates, we calculated the number of exchange events in which C10 molecules transitioned between the aggregated state and the free monomeric state. For each frame, molecules were classified as either part of an aggregate or as isolated monomers in the aqueous phase. By tracking changes in these classifications between successive snapshots, we identified expulsion (aggregate → monomer) and insertion (monomer → aggregate) events. These transitions were quantified over the final 10 snapshots of each simulation, and the mean and standard deviation were calculated for all systems. The results are summarized in Fig. 6.

A striking difference was observed between the two force fields. For every corresponding condition, Martini 3 produced approximately five- to seven-fold more expulsion and insertion events than Martini 2. This clearly demonstrates that Martini 3 captures a far more dynamic aggregation environment, while Martini 2 predicts markedly slower molecular exchange. The suppressed dynamics in Martini 2 align with its tendency to produce fewer free monomers, and fewer number of aggregates

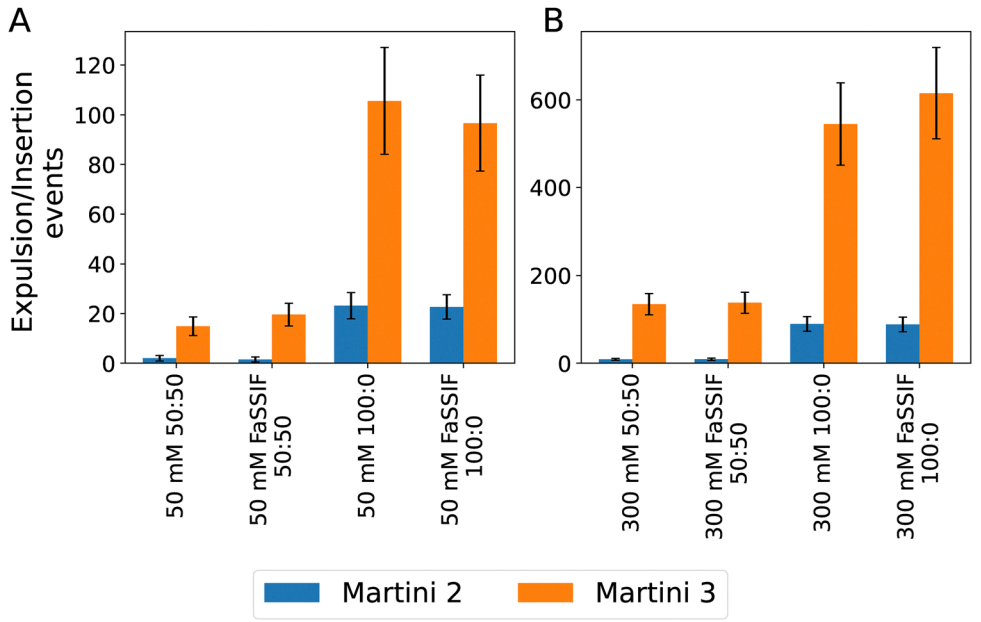

Fig. 6 Average number of expulsion and insertion events calculated from the final ten snapshots of the simulated systems representing 50 ns of the simulation time for (A) 50 mM C10 and (B) 300 mM C10 in phosphate buffer.

observed in the previous sections. Also, higher concentration systems (300 mM) showed elevated numbers of exchange events relative to their 50 mM counterparts, consistent with the greater availability of molecules capable of participating in insertion and expulsion processes.

Across all conditions, the number of exchange events was substantially higher at pH 8.5 than at pH 6.5. This indicates that, in addition to forming smaller micellar structures, the high-pH systems exhibit more pronounced dynamic behavior, with frequent exchange of C10 molecules between micelles and the surrounding solution. This pH-dependent increase in exchange dynamics is also notable in a broader context. Dahlgren *et al.*[32] reported an 8–9-fold increase in enalaprilat permeability in the presence of C10 at physiological pH, whereas almost no enhancement was observed at pH 6.5. While the free monomer pool is suggested to be the key contributor to this effect, our results suggest that micelle dynamics themselves—that is, how rapidly molecules detach from and re-associate with aggregates—may also influence how effectively C10 can interact with and perturb epithelial membranes. Taken together, the higher exchange activity captured by Martini 3 provides a mechanistic picture that is more consistent with experimentally observed pH-dependent permeation behavior, whereas Martini 2 underestimates both the mobility and availability of C10 needed to drive such effects.

3.5. Martini 3 provides a better match to experimental SAXS profiles than Martini 2

To validate the aggregate sizes and morphologies predicted by our simulations, we first performed dynamic light scattering (DLS) measurements on systems containing 300 mM C10 at pH 6.5 and pH 8.5 (Fig. 7A). At pH 6.5, the DLS results showed a broad size distribution with an average radius of approximately 700 nm and a polydispersity index (PDI) of 0.45, indicating the presence of large, heterogeneous aggregates, and consistent with the simulation results at this pH. In contrast, the pH 8.5 sample displayed a dominant, narrow peak corresponding to an average radius of approximately 2 nm (with PDI 0.45), characteristic of small spherical micelles. A secondary, weaker peak near 100 nm was also detected, likely arising from transient clustering of smaller micelles rather than discrete, compact aggregates. The DLS measurements align well with the observations of Berg *et al.*,[18] who also reported similar size behavior under comparable conditions.

To further characterize these systems, we collected small-angle X-ray scattering (SAXS) profiles for the same conditions. The SAXS curves revealed clear pH-dependent differences: at pH 6.5, the scattering intensity was substantially higher, consistent with the coexistence of larger colloidal structures alongside smaller micelles. Aggregation, even pre-micellar below CMC,[16] is known to raise the apparent pK_a of fatty acids, so at this pH the molecules are partly charged and partly uncharged, a mixed state that promotes formation of these larger aggregates. In contrast, at pH 8.5, where the molecules are almost fully charged, the SAXS profile exhibited a characteristic decay and oscillation pattern indicative of the presence of small, well-defined spherical micelles. The increased repulsion among the highly charged molecules at pH 8.5 likely reduces intermolecular interactions, thus favoring smaller, more uniform micellar structures.

To determine which coarse-grained model better captures these experimentally observed scattering features, we calculated theoretical SAXS curves for both Martini 2 and Martini 3 using Pepsi-SAXS (Fig. 7B).[24] The comparison between

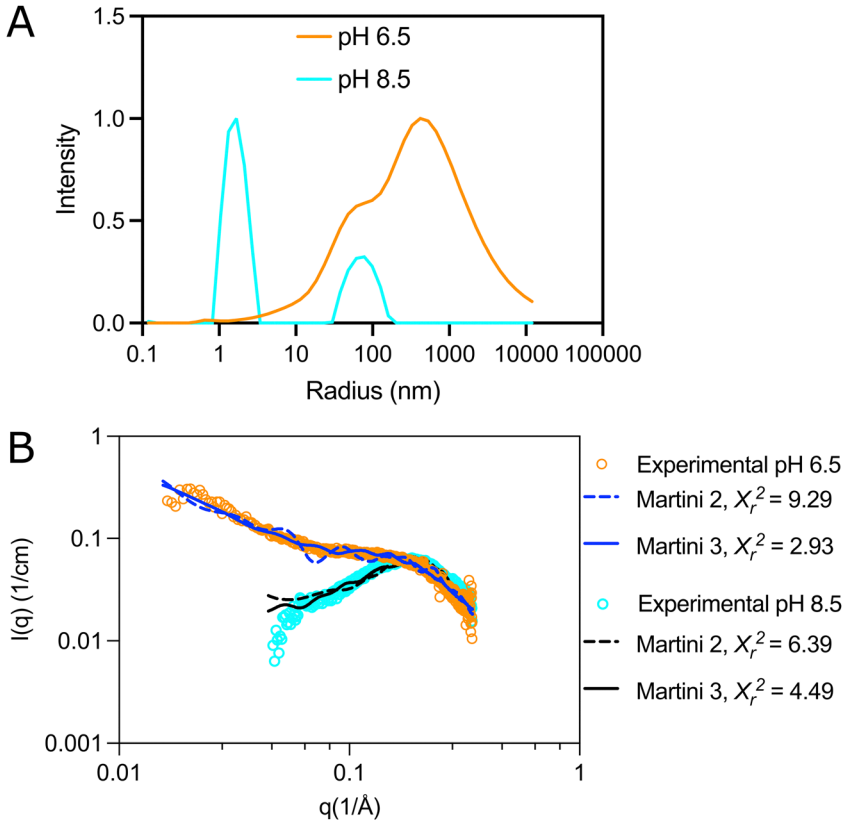

Fig. 7 Dynamic light scattering (DLS) intensity profiles and theoretical SAXS spectra for the 300 mM C10 systems at different pH conditions. (A) DLS measurements showing the particle size distribution for the 300 mM C10 system at pH 6.5 and 8.5 (B) Theoretical SAXS spectra calculated using Pepsi-SAXS for Martini 3 and Martini 2 simulations, compared with experimental SAXS data at pH 6.5 and 8.5. The reduced square (Xr^2) reports the goodness of fit between theoretical and experimental scattering profiles.

simulated and experimental profiles reveals a clear performance difference between the two force fields. Although neither model achieved a reduced chi-square (Xr^2) below 1, Martini 3 consistently produced substantially lower Xr^2 values across both pH conditions, indicating a significantly better overall fit. Note that, Xr^2 close to or below 1 indicates that the theoretical model adequately describes the experimental data, reflecting good agreement within the expected uncertainties. At pH 6.5, Martini 3 yielded a Xr^2 of 2.93 (χ^2 = 1.71), whereas Martini 2 produced a considerably poorer fit with Xr^2 = 4.87 (χ^2 = 3.05). A similar trend was observed at pH 8.5, where Martini 3 achieved Xr^2 = 4.49 (χ^2 = 2.12), again outperforming Martini 2, which showed Xr^2 = 6.32 (χ^2 = 2.52).

A visual inspection of the scattering curves further underscores these differences. Martini 3 showed notably closer alignment with the experimental SAXS intensity decay, especially within the q-range of approximately 0.04–0.16 Å^{-1}, where Martini 2 exhibited pronounced deviations. These results collectively demonstrate that Martini 3 represents C10 aggregate structure more accurately, likely due to its improved parametrization of amphiphile packing and solvation interactions. Such enhanced agreement is crucial for simulations intended to support SAXS interpretations or guide formulation design.

Future improvements to the theoretical scattering calculations could involve adaptive sampling, ensemble modeling, or parameter refinement to further reduce discrepancies and better account for aggregate heterogeneity.

4. Conclusion

In this study, we combined coarse-grained molecular dynamics (CG-MD) simulations with SAXS and DLS experiments to investigate the pH- and concentration-dependent self-assembly of sodium caprate (C10) in aqueous buffer and in the presence of fasted-state simulated intestinal fluid (FaSSIF). At pH 6.5, both simulations and experiments revealed the formation of large, heterogeneous colloidal aggregates, reflecting strong intermolecular attractions when C10 is partially protonated. At pH 8.5, where all C10 molecules are deprotonated, interactions weakened and small spherical micelles predominated. These structural trends were consistently captured by both simulation and experiment.

FaSSIF further modulated C10 aggregation, with effects that differed substantially between the force fields. At low pH, FaSSIF altered both the number of molecules per cluster and the overall cluster population, most prominently in Martini 3. At high pH, FaSSIF increased the fraction of spherical micelles in Martini 2 but decreased it in Martini 3, underscoring fundamental differences in how the two force fields represent amphiphile–solvent interactions.

Across all structural and dynamic analyses, including cluster-size distributions, number of molecules per aggregate, percentage of free monomers, eccentricity profiles, and monomer–aggregate exchange rates, Martini 2 and Martini 3 produced markedly different behaviors. Martini 2 consistently formed more rigid, compact, slowly exchanging aggregates and underpredicted the availability of free monomers compared to solubility-based theoretical prediction, whereas Martini 3 generated highly dynamic assemblies with substantially higher insertion and expulsion events. In addition, the theoretical SAXS profiles derived from Martini 3 showed significantly better agreement with experimental data, yielding lower χ^2 values and a more accurate representation of the characteristic intensity decay across the relevant q-range. In contrast, Martini 2 deviated more noticeably from the experimental curves, particularly in regions sensitive to micelle shape and internal density fluctuations.

Overall, these findings show that Martini 3 not only reproduces the experimental structural features more accurately, but also captures a more realistic dynamic behavior of C10 aggregates. This is important because micelle–monomer exchange may directly influence how released C10 molecules interact with surrounding biological components, such as lipid membranes, rather than simply re-entering other aggregates. Accurately describing this dynamic equilibrium is therefore essential for understanding C10 behavior under physiologically relevant conditions and for the rational design of amphiphile-based drug delivery systems. Overall, our findings highlight the value of combining CG-MD simulations with scattering techniques to obtain robust molecular-level insight into amphiphile aggregation. They also emphasize the need for careful force-field selection and experimental validation when applying simulations to pharmaceutical formulation development and to the broader physical chemistry of self-assembling systems.

Author contributions

SA performed the experiments. SA and SH conducted the formal analysis and investigation, prepared visualizations, and wrote the original draft. LMB contributed to the investigation, supervised the work, and participated in reviewing and editing the manuscript. PH contributed to the investigation, provided resources, and participated in reviewing and editing the manuscript. PL contributed to the conceptualization, resources, and investigation, participated in reviewing and editing the manuscript, and acquired funding. All authors read and approved the final manuscript.

Conflicts of interest

The authors declare that they have no competing interests.

Data availability

The datasets (scattering data and final simulation snapshots) generated and/or analysed during the current study are available in the figshare repository, https://figshare.com/s/c367a09316913ba3b2ea.

Supplementary information (SI) is available. See DOI: https://doi.org/10.1039/d6cp00414h.

Acknowledgements

The authors acknowledge financial support from Swedish National Graduate School in Neutron Scattering (SwedNess), Swedish Foundation for Strategic Research (SSF) GSn15 – 0008. Also, financial support from VINNOVA (2019-00048) for the Swedish Drug Delivery Center (SweDeliver) is gratefully acknowledged. The computations were enabled by resources provided by the National Academic Infrastructure for Supercomputing in Sweden (NAISS), partially funded by the Swedish Research Council through grant agreement no. 2022-06725. We are thankful to the Department of Medicinal Chemistry at Uppsala University for access to the SAXS instrument. This work benefited from the use of the SasView application, originally developed under NSF award DMR-0520547. SasView contains code developed with funding from the European Union's Horizon 2020 research and innovation programme under the SINE2020 project, grant agreement No 654000.

References

1 P. Li, H. M. Nielsen and A. Müllertz, Oral delivery of peptides and proteins using lipid-based drug delivery systems, *Expert Opin. Drug Delivery*, 2012, **9**(10), 1289–1304.
2 S. Maher, *et al.*, Application of Permeation Enhancers in Oral Delivery of Macromolecules: An Update, *Pharmaceutics*, 2019, **11**, 1.
3 M. Nicze, *et al.*, The Current and Promising Oral Delivery Methods for Protein- and Peptide-Based Drugs, *Int. J. Mol. Sci.*, 2024, **25**(2), 815.
4 S. M. Krug, *et al.*, Sodium caprate as an enhancer of macromolecule permeation across tricellular tight junctions of intestinal cells, *Biomaterials*, 2013, **34**(1), 275–282.
5 M. A. Karsdal, *et al.*, Lessons learned from the clinical development of oral peptides, *Br. J. Clin. Pharmacol.*, 2015, **79**(5), 720–732.
6 S. Maher, R. J. Mrsny and D. J. Brayden, Intestinal permeation enhancers for oral peptide delivery, *Adv. Drug Delivery Rev.*, 2016, **106**, 277–319.
7 M. Tomita, M. Hayashi and S. Awazu, Absorption-Enhancing Mechanism of EDTA, Caprate, and Decanoylcarnitine in Caco-2 Cells, *J. Pharm. Sci.*, 1996, **85**(6), 608–611.
8 D. J. Brayden and S. Maher, Transient Permeation Enhancer® (TPE®) technology for oral delivery of octreotide: a technological evaluation, *Expert Opin. Drug Delivery*, 2021, **18**(10), 1501–1512.
9 J. R. Burnett and A. J. Hooper, MK-0616: an oral PCSK9 inhibitor for hypercholesterolemia treatment, *Expert Opin. Invest. Drugs*, 2023, **32**(10), 873–878.

10 E. Zhang, H. Z. Boyi Song, Y. Shi and Z. Cao, Recent advances in oral insulin delivery technologies, *J. Controlled Release*, 2024, **366**, 221–230.
11 S. Maher, R. J. Mrsny and D. J. Brayden, Intestinal permeation enhancers for oral peptide delivery, *Adv. Drug Delivery Rev.*, 2016, **106**(Pt B), 277–319.
12 R. Kneiszl, S. Hossain and P. Larsson, In Silico-Based Experiments on Mechanistic Interactions between Several Intestinal Permeation Enhancers with a Lipid Bilayer Model, *Mol. Pharmaceutics*, 2022, **19**(1), 124–137.
13 S. Hossain, *et al.*, Influence of Bile Composition on Membrane Incorporation of Transient Permeability Enhancers, *Mol. Pharmaceutics*, 2020, **17**(11), 4226–4240.
14 S. Maher, *et al.*, Application of Permeation Enhancers in Oral Delivery of Macromolecules: An Update, *Pharmaceutics*, 2019, **11**, 41.
15 M. S. Hossain, *et al.*, Aggregation Behavior of Medium Chain Fatty Acids Studied by Coarse-Grained Molecular Dynamics Simulation, *AAPS PharmSciTech*, 2019, **20**, 61.
16 J. R. Kanicky and D. O. Shah, Effect of Premicellar Aggregation on the pK_a of Fatty Acid Soap Solutions, *Langmuir*, 2003, **19**(6), 2034–2038.
17 T. Namani and P. Walde, From Decanoate Micelles to Decanoic Acid/Dodecylbenzenesulfonate Vesicles, *Langmuir*, 2005, **21**(14), 6210–6219.
18 S. Berg, *et al.*, Impact of Intestinal Concentration and Colloidal Structure on the Permeation-Enhancing Efficiency of Sodium Caprate in the Rat, *Mol. Pharmaceutics*, 2022, **19**(1), 200–212.
19 S. J. Marrink, A. H. de Vries and A. E. Mark, Coarse Grained Model for Semiquantitative Lipid Simulations, *J. Phys. Chem. B*, 2004, **108**(2), 750–760.
20 S. Kmiecik, *et al.*, Coarse-Grained Protein Models and Their Applications, *Chem. Rev.*, 2016, **116**(14), 7898–7936.
21 E. Negro, *et al.*, Experimental and molecular dynamics characterization of dense microemulsion systems: morphology, conductivity and SAXS, *Soft Matter*, 2014, **10**(43), 8685–8697.
22 M. S. Hossain, *et al.*, Aggregation Behavior of Medium Chain Fatty Acids Studied by Coarse-Grained Molecular Dynamics Simulation, *AAPS PharmSciTech*, 2019, **20**(2), 61.
23 T. Ekimoto, *et al.*, Combination of coarse-grained molecular dynamics simulations and small-angle X-ray scattering experiments, *Biophys. Physicobiol.*, 2019, **16**, 377–390.
24 S. Grudinin, A. Martel and S. Prevost, Pepsi-SAXS/SANS -small-angle scattering-guided tools for integrative structural bioinformatics, *Acta Crystallogr., Sect. A: Found. Adv.*, 2021, **77**(A2), C49.
25 S. J. Marrink, *et al.*, The MARTINI Force Field: Coarse Grained Model for Biomolecular Simulations, *J. Phys. Chem. B*, 2007, **111**(27), 7812.
26 R. Alessandri, *et al.*, Martini 3 Coarse-Grained Force Field: Small Molecules, *Adv. Theory Simul.*, 2022, **5**(1), 2100391.
27 A. J. Clulow, *et al.*, Characterization of Solubilizing Nanoaggregates Present in Different Versions of Simulated Intestinal Fluid, *J. Phys. Chem. B*, 2017, **121**(48), 10869–10881.
28 S. Hossain, *et al.*, Explicit-pH Coarse-Grained Molecular Dynamics Simulations Enable Insights into Restructuring of Intestinal Colloidal Aggregates with Permeation Enhancers, *Processes*, 2022, **10**(1), 29.
29 G. Bussi, D. Donadio and M. Parrinello, Canonical sampling through velocity rescaling, *J. Chem. Phys.*, 2007, **126**, 1.
30 M. J. Abraham, *et al.*, GROMACS: High performance molecular simulations through multi-level parallelism from laptops to supercomputers, *SoftwareX*, 2015, **1–2**, 19–25.
31 T. A. Wassenaar, *et al.*, Going Backward: A Flexible Geometric Approach to Reverse Transformation from Coarse Grained to Atomistic Models, *J. Chem. Theory Comput.*, 2014, **10**(2), 676–690.
32 D. Dahlgren, *et al.*, The In Vivo Effect of Transcellular Permeation Enhancers on the Intestinal Permeability of Two Peptide Drugs Enalaprilat and Hexarelin, *Pharmaceutics*, 2020, **12**(2), 99.
33 A. Majumder and J. E. Straub, Addressing the Excessive Aggregation of Membrane Proteins in the MARTINI Model, *J. Chem. Theory Comput.*, 2021, **17**(4), 2513–2521.
34 X. Periole, Interplay of G Protein-Coupled Receptors with the Membrane: Insights from Supra-Atomic Coarse Grain Molecular Dynamics Simulations, *Chem. Rev.*, 2017, **117**(1), 156–185.
35 T. A. Dunton, *et al.*, The Free Energy Landscape of Dimerization of a Membrane Protein, NanC, *PLoS Comput. Biol.*, 2014, **10**(1), e1003417.
36 M. Heidari, M. Sikora and G. Hummer, Refined Protein–Sugar Interactions in the Martini Force Field, *J. Chem. Theory Comput.*, 2024, **20**(22), 10259–10265.
37 R. Alessandri, *et al.*, Pitfalls of the Martini Model, *J. Chem. Theory Comput.*, 2019, **15**(10), 5448–5460.
38 F. Grunewald, *et al.*, Martini 3 Coarse-Grained Force Field for Carbohydrates, *J. Chem. Theory Comput.*, 2022, **18**(12), 7555–7569.

